

The Role of Turbulence in Fueling the Subsurface Chlorophyll Maximum in Tidally Dominated Shelf Seas

**Key Points:**

- Turbulence and chlorophyll both peak at the base of the pycnocline on a mid-latitude shelf
- Locally generated turbulence at the pycnocline base is a fuel pump for the subsurface chlorophyll maximum
- Amplitude and polarity of the M2 tide govern the local generation of turbulence at the pycnocline base

Correspondence to:

J. Becherer,
johannes.becherer@hereon.de

Citation:

Becherer, J., Burchard, H., Carpenter, J. R., Graewe, U., & Merckelbach, L. M. (2022). The role of turbulence in fueling the subsurface chlorophyll maximum in tidally dominated shelf seas. *Journal of Geophysical Research: Oceans*, 127, e2022JC018561. <https://doi.org/10.1029/2022JC018561>

Received 16 FEB 2022

Accepted 16 AUG 2022

The copyright line for this article was changed on 2 SEP 2022 after original online publication.

Johannes Becherer¹ , Hans Burchard² , Jeffrey R. Carpenter¹ , Ulf Graewe², and Lucas M. Merckelbach¹

¹Helmholtz-Center Hereon, Geesthacht, Germany, ²Leibniz Institute for Baltic Sea Research Warnemünde, Rostock, Germany

Abstract Glider observations show a subsurface chlorophyll maximum (SCM) at the base of the seasonal pycnocline in the North Sea during stable summer conditions. A collocated peak in the dissipation rate of turbulent kinetic energy suggests the presence of active turbulence that potentially generates a nutrient flux to fuel the SCM. A one-dimensional turbulence closure model is used to investigate the dynamics behind this local maximum in turbulent dissipation at the base of the pycnocline (PCB) as well as its associated nutrient fluxes. Based on a number of increasingly idealized forcing setups of the model, we are able to draw the following conclusions: (a) only turbulence generated inside the stratified PCB is able to entrain a tracer (e.g., nutrients) from the bottom mixed layer into the SCM region; (b) surface wind forcing only plays a secondary role during stable summer conditions; (c) interfacial shear from the tide accounts for the majority of turbulence production at the PCB; (d) in stable summer conditions, the strength of the turbulent diapycnal fluxes at the PCB is set by the strength of the anticyclonic component of the tidal currents.

Plain Language Summary Many midlatitude shelf seas are vertically stratified in summer, where a warm surface layer sits on top of a cold, dense bottom layer. Both of these layers are unproductive environments for phytoplankton—the bottom layer is light limited, and the surface layer is nutrient-limited. However, abundant phytoplankton is observed directly at the interface between surface and bottom layers. In order to sustain this phytoplankton, nutrient-rich bottom water needs to be mixed with interface water. While both wind and tides are major causes for mixing in the coastal ocean, we find that the tides alone provide sufficient stirring at the right place to potentially act as an effective fuel pump for the phytoplankton. Interestingly, it is not the strength of the tides alone that counts, rather the sense of rotation of the tidal currents; rotation opposite to the Earth's spin causes more stirring than rotation along with it.

1. Introduction

Continental shelf seas are very energetic environments, dissipating about two thirds of the global tidal energy (Egbert & Ray, 2000) despite accounting for less than 11% of the ocean's surface and less than 1% of its water volume. Their highly productive ecosystems give rise to a disproportionately large fraction of the global ocean's primary production (Muller-Karger et al., 2005). Due to a combination of processes referred to as the *shelf sea pump* (Tsunogai et al., 1999), the coastal ocean plays a vital role in the uptake and export of CO₂ from the atmosphere, which makes it a key element in Earth's climate system (Bianchi et al., 2005; Borges et al., 2005; Muller-Karger et al., 2005; Thomas et al., 2004).

Vertical stratification is one of the major physical controls on the shelf's primary production and ability to export carbon. In midlatitude regions, extended areas of the shelf are subject to seasonal density stratification (Berk & Hughes, 2009; van Leeuwen et al., 2015) with well-mixed conditions in winter and a stably stratified water column in summer. During the transition between these two seasons, in spring, solar heating generates a warm and therefore less dense surface layer. The light exposure in this shallow surface layer in concert with high nutrient concentrations yield strong algae growth that marks the main primary production event of the year, the spring bloom (see May–June in Figure 1). On the flip side, constant solar heating throughout spring increases stratification, inhibiting vertical turbulent transport, which effectively decouples the surface from the bottom layer. The strong primary production of the spring bloom quickly consumes all nutrients in the surface layer. The result is a typical summer situation with a warm, nutrient-poor surface layer on top of a cold, relatively nutrient-rich bottom layer (Figure 2). Both layers are limited in primary production, the surface layer due to nutrient deficiency and the bottom layer due to missing light exposure. Relatively low surface chlorophyll concentrations in summer are

© 2022. The Authors.

This is an open access article under the terms of the [Creative Commons Attribution License](https://creativecommons.org/licenses/by/4.0/), which permits use, distribution and reproduction in any medium, provided the original work is properly cited.

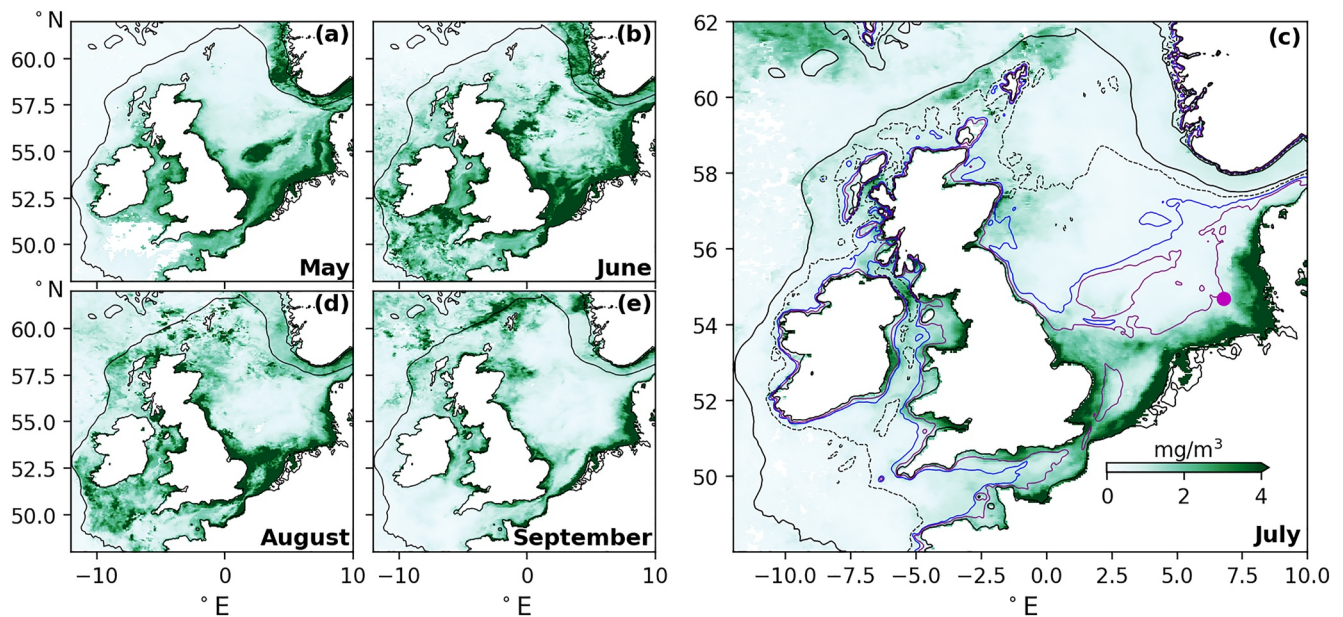


Figure 1. Monthly averaged sea surface chlorophyll concentration of the northwest European shelf obtained from satellite (NASA Ocean Biology Processing Group, 2017) in 2014. Magenta dot in (c) indicates the measurement location. In panel (c), different isobaths are indicated (purple 40 m, blue 60 m, black dashed 100 m, and black solid 200 m).

a clear indication of unfavorable conditions for primary production in vast areas of the surface layer of the North Sea (July–September Figure 1).

The bottom and surface layers are separated by a pycnocline region, whose vertical extent can be limited to a few meters. Despite inhibiting conditions for primary production in the surface and bottom layers, observations indicate the presence of a distinct subsurface chlorophyll maximum (SCM) inside the pycnocline that persists throughout the stratified season (Cullen, 2015; Richardson et al., 2000). It has been suggested that this SCM is the main source region for primary production during the stratified summer months (Richardson et al., 2000). Integrated over the entire year, the relatively slower primary production inside the SCM can even outweigh the rapid but short-lived production generated by the spring bloom (Richardson et al., 2000). As a persistent feature

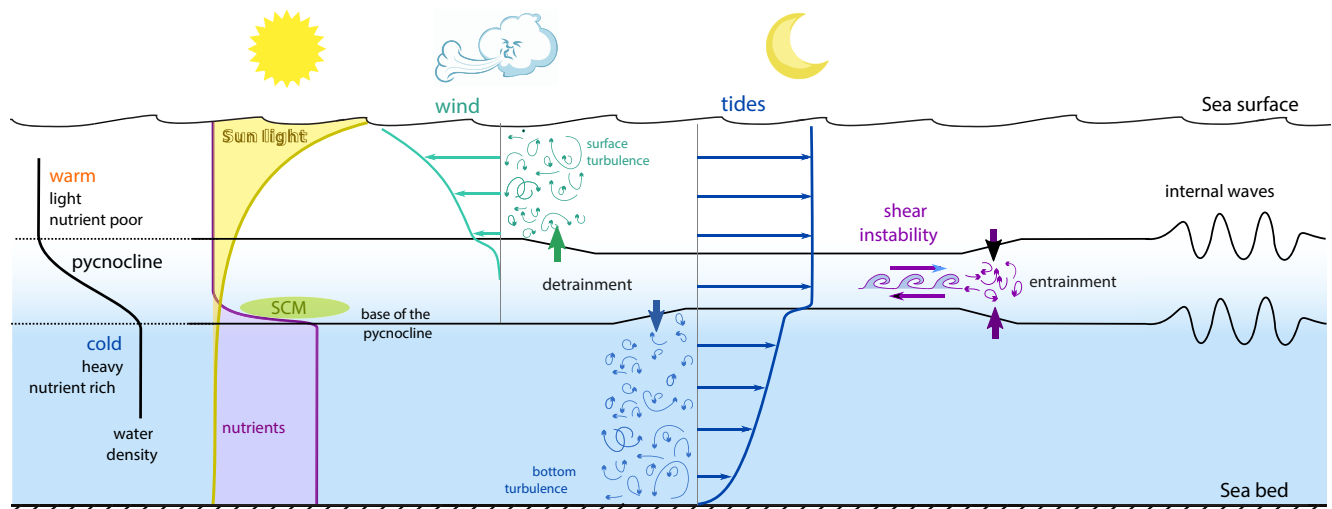


Figure 2. Conceptual sketch of the water column of seasonally stratified shelf seas with a warm nutrient-poor surface layer and a cold nutrient-rich bottom layer separated by a pycnocline, which is habitat to the subsurface chlorophyll maximum (SCM). The main forcing agents are winds, tides, and internal waves, which all yield turbulent mixing in different parts of the water column.

during the stratified summer months, the SCM is potentially an important component of the shelf sea's CO₂ pump (T. Rippeth et al., 2014; Thomas et al., 2004). Therefore, investigating the dynamical controls on the SCM is crucial both to understand the local ecosystem and the overall role of shelf seas as major carbon sinks in Earth's climate system.

Observations indicate that the SCM mainly occurs at the base of the pycnocline, which coincides with the nutricline, that is, the region with the strongest gradient in nutrients (Cullen, 2015; Sharples, Moore, Rippeth, et al., 2001). Here, the light intensity is already significantly reduced compared to the surface layer (Sharples, Moore, Rippeth, et al., 2001). However, its vicinity to the nutrients in the bottom layer is necessary for primary production. Moore et al. (2006) demonstrated that the SCM in shelf seas does in fact correspond to a true maximum in biomass and not just an increased photoacclimation response. To avoid being mixed to the bottom, neutrally buoyant phytoplankton constituting the SCM must retain within the stratified pycnocline. Turbulent nutrient flux from the well-mixed bottom layer (BML) into the stratified base of the pycnocline is one of the primary physical controls of the growth of the SCM.

In tidally dominated shelf seas, there are three distinct turbulence production regions in the water column (Figure 2): (a) the sea surface, due to direct wind stress and breaking waves, (b) the sea bed, due to friction of mean and tidal currents with the bed, and (c) the pycnocline itself, due to intermittent shear instabilities (T. P. Rippeth et al., 2005; Sharples, Moore, Rippeth, et al., 2001). In this paper, we will demonstrate that strong shear in particular, at the base of the pycnocline, generates turbulence that can entrain a tracer (e.g., nutrients) from the BML into the pycnocline.

The potential importance of shear instabilities inside the pycnocline for diapycnal mixing in shelf seas was the subject of many groundbreaking studies during the last two decades (e.g., van Haren et al., 1999; T. P. Rippeth et al., 2005; Sharples, Moore, Rippeth, et al., 2001; Palmer et al., 2008; Burchard & Rippeth, 2009; Lincoln et al., 2016). Several different physical processes were identified to play leading roles in generating strong shear inside the pycnocline, among which are internal tides (Becherer et al., 2021a, 2021b; Green et al., 2010; Sharples, Moore, & Abraham, 2001; Sharples & Zeldis, 2019), inertial oscillations (van Haren et al., 1999; Williams et al., 2013), high-frequency internal waves (Inall et al., 2000; MacKinnon & Gregg, 2003; T. P. Rippeth, 2005; Palmer et al., 2008) as well as the barotropic tide itself (Maas & van Haren, 1987; Souza & Simpson, 1996; van Haren, 2000).

Interactions of these individual processes were found to be of great importance for pycnocline stability as well. For instance, the alignment of wind stress, bottom stress, and bulk shear is able to generate shear spikes, which can yield strong intermittent mixing events in the pycnocline (Burchard & Rippeth, 2009; Williams et al., 2013). van Haren et al. (1999) show that substantial peaks in the baroclinic energy spectrum can be found not only at the main forcing frequencies f (Coriolis frequency) and ω_{m_2} (M_2 tidal frequency), but also at their beat frequency ($\omega_{m_2} - f$), pointing toward substantial interactions of the inertial waves and the internal tide. It has been hypothesized that all these processes taken together keep the pycnocline on average in a state of marginal stability, where little extra shear can yield significant mixing (van Haren et al., 1999; T. P. Rippeth, 2005; T. P. Rippeth et al., 2009).

Here, we will attempt to systematically identify the leading order processes that are able to generate turbulence specifically at the base of the pycnocline, since these are crucial for fluxing nutrients from the BML into the pycnocline and hence for fueling the SCM. We will demonstrate that in calm summer conditions, the barotropic tide alone can account for most of the turbulence production at the base of the pycnocline seen in our observations. Shear from the barotropic tide will be particularly effective in fluxing tracers from the BML into the pycnocline, since it is primarily focused right at the base of the pycnocline. Furthermore, we will show that not just the strength of the tidal currents, but more importantly its polarity is key for generating strong turbulence at the base of the pycnocline. At least during calm summer conditions, the influence of wind is found to be less important.

2. Observation

2.1. Field Experiment

The observations presented in this paper were taken during a field campaign in the German Bight (magenta dot in Figure 1c) in the summer of 2014. An upward looking Doppler current profiler (ADCP, RDI Workhorse Sentinel,

600 kHz) was positioned in 39.5 m depth at the sea bed (54.68°N, 6.78°E) and configured to collect 30 ping ensembles at 10-min intervals. The bin size was set to 0.4 m.

Concurrently, an ocean glider (Shallow (100 m) from Teledyne Webb Research Slocum Electric) was deployed from day 209 (28 July) to 230 (18 August) of 2014. The glider was programmed such that casts span 0.5–1.0 m from the surface to 2.0–2.5 m from the sea bed, resulting in roughly 15 casts every 3 hr before surfacing. Beginning from day 216 (4 August), the glider was configured to spiral by setting the rudder fin to 0.2 rad, causing the glider to make a full circle in 450–500 s. In this mode, the glider passively drifts with the tides providing a close to Lagrangian view of the water column. During this time, the glider stayed within a distance of less than 20 km from the ADCP's location.

The focal period of this paper is between days 216 and 221 of 2014, where the glider spirals close to the ADCP through a summer stratified water column in calm weather during neap tide conditions. After day 221 (9 August), a storm hits the area, yielding strong vertical mixing, which is described in Schultze et al. (2020).

The glider was equipped with a CTD (Seabird SBE41, 0.5 Hz sample rate) to measure density and pressure as well as an optical turbidity and fluorescence sensor (Wetlabs FLNTU, 1 Hz sample rate) besides a variety of other sensors that will not be further discussed here (see Schultze et al., 2017).

Attached to the glider was a turbulence package (MicroRider-1000LP, Rockland Scientific International), which allowed direct estimates of the dissipation rate of turbulent kinetic energy, ϵ , via two shear probes (SPM-38, 512 Hz) based on the methods described by Fer et al. (2014), Lueck et al. (2002), Schultze et al. (2017), Wolk et al. (2002). An analysis of the entire data set, as well as a detailed discussion of the turbulence measurements, can be found in Schultze et al. (2017). For reasons of consistency, we only use here turbulence estimates from glider downcasts, since Schultze et al. (2017) noted a slight systematic discrepancy in vertical profiles of ϵ between up- and downcasts in the pycnocline.

We have no direct nutrient measurements available. However, a climatology (Hinrichs et al., 2017) suggests that near-bottom concentrations of nitrate (1.5–5 mmol/m³) are usually between 3 and 10 times larger than those at the surface (<0.5 mmol/m³) throughout July close to our study site. This difference becomes less pronounced during August as the first fall storms mix the water column. Our observation period at the beginning of August is just before the first such wind event, which makes July conditions the most representative for the data set presented here.

2.2. Density Stratification

Up to day 221 (August 9) of 2014, the water column is characterized by a two-layer structure, with a warm, slightly fresher surface layer on top of a colder slightly more saline bottom layer (Figure 3b). In between is a strongly stratified pycnocline, which we define as the region containing 90% of the density variation (gray lines, Figure 3, see also Schultze et al. (2020) for a comparison of different definitions).

At day 221 (August 9), a storm over the region, with wind speeds above 15 m s⁻¹ (Figure 3a), causes strong mixing, eventually leading to a well-mixed water column after year day 223. This mixing event marks the end of the stratified summer period and the beginning of the well-mixed winter season.

Here, we are interested in typical summer conditions in the North Sea as a model for seasonally stratified shelf seas in general. Therefore, we focus on a relatively stable pre-storm period. To this end, we present vertical profiles (Figure 4) that are time averages over year days 216.4–217.95 (see magenta box, Figure 3b). This period is short enough to provide reasonable averages, but at the same time it covers three M_2 tidal cycles to avoid aliasing of the tidal signal. Furthermore, the wind speeds are relatively low during this period (see Figure 3a), in line with our intentions to concentrate on typical summer background conditions without any major wind forcing.

2.3. Chlorophyll Maximum

Figure 3c shows the signal of the fluorescence sensor onboard of the glider in mg/m³. However, we did not attempt any calibration in terms of actual chlorophyll concentrations or biomass, nor did we correct for daylight contamination. Therefore, these data cannot be used to make any quantitative estimates. Nevertheless, we are able to derive a number of important qualitative observations.

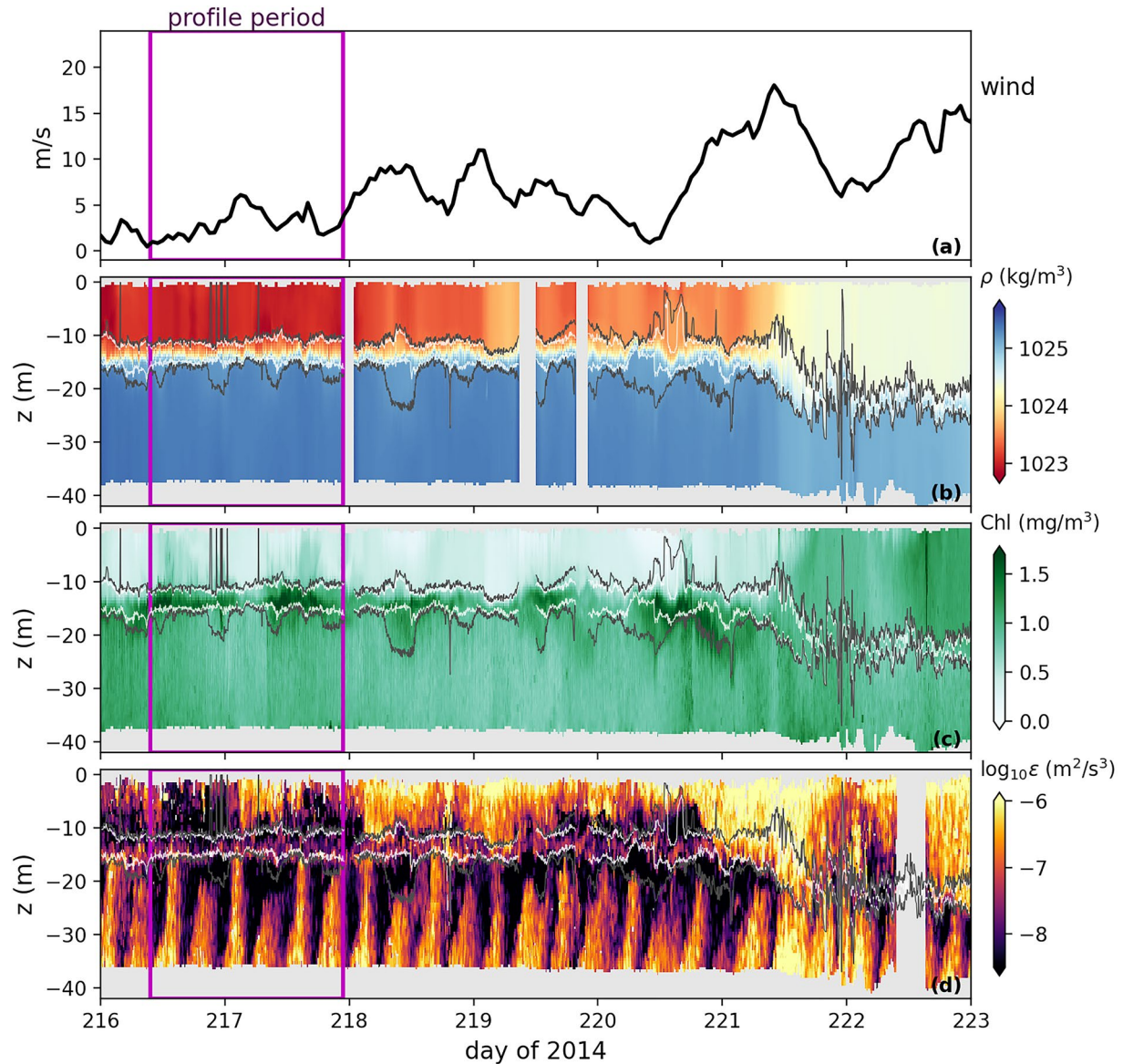


Figure 3. Observations. (a) Wind speed from Cosmo Reanalysis (Kaspar et al., 2020) (b) density, (c) Chlorophyll-a (uncalibrated), and (d) dissipation of turbulent kinetic energy. The white and gray lines mark the pycnocline, defined here as the region containing 90% (gray) and 80% (white) of the density variation (same definition as in Schultze et al. (2020)).

During the stratified pre-storm period, the upper layer is characterized by relatively low chlorophyll concentrations (Figure 4b), indicating nutrient deficiency in the near-surface photic zone. The bottom layer has higher chlorophyll concentrations than the surface despite significantly less light exposure. The highest chlorophyll concentrations in the water column are found at the base of the pycnocline just above the lower dashed line in Figure 4b. This well-established SCM coincides with the lower part of the strongly stratified pycnocline region (compare Figures 4a and 4b), directly above the presumably nutrient-rich, well-mixed bottom waters.

Strong mixing in connection to the storm event yields a clear increase of near-surface chlorophyll concentrations following day 221 (Figure 3c). This increase appears to be primarily due to vertical redistribution of phytoplankton since the depth-average chlorophyll concentration does not significantly change. During the following well-mixed period, the chlorophyll signal is vertically homogeneous without any clear signature of an SCM (not shown). A more detailed analysis of the storm-induced mixing event can be found in Schultze et al. (2020).

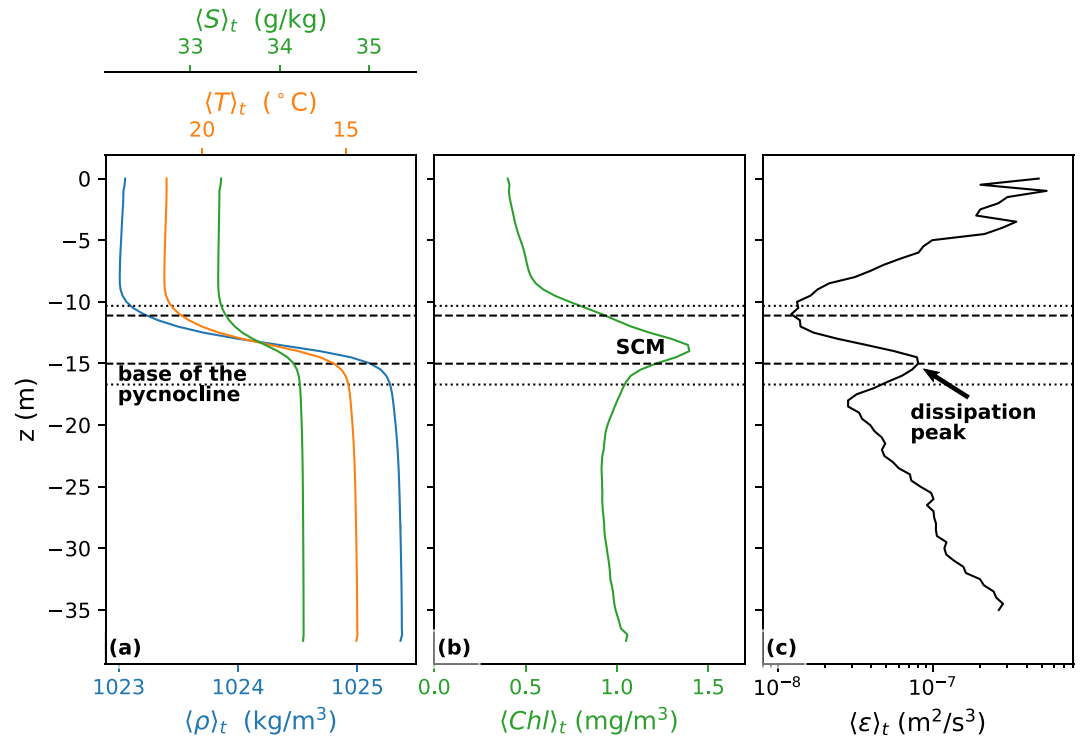


Figure 4. Vertical profiles time-averaged ($\langle \cdot \rangle_t$) between year day 216.4 and 217.95, covering three tidal cycles during a period with weak winds (magenta box in Figure 3b). (a) Density (blue), temperature (orange), and salinity (green), (b) Chlorophyll-a (uncalibrated), and (c) dissipation of turbulent kinetic energy. Black horizontal lines indicate 80% (dashed) and 90% (dotted) criteria for pycnocline position. In (a) the axes have been scaled so that they correspond to equal changes in density.

2.4. Turbulence Observations

During the pre-storm phase (before day 221), we can identify three vertically distinct turbulence generation regions (Figure 3d). In the surface layer, extended periods of high dissipation levels are likely linked to intermittent wind forcing, generating turbulence due to surface shear stresses and wave breaking (compare Figures 3a and 3d). In contrast, the bottom layer is characterized by periodically reoccurring (quarter-diurnal) dissipation events, which are intensified toward the bed, implying turbulence generated by bottom friction due to tidal currents.

The third region of enhanced turbulence coincides with the base of the pycnocline (see lower white line in Figure 3d). In the average profile (Figure 4c), we see a clear local maximum of dissipation coinciding with the lower edge of the pycnocline (dashed line). Here, dissipation levels are clearly elevated over the neighboring upper bottom layer and the center pycnocline region. This indicates that dissipation observed here is not just due to vertical transport of bottom-generated turbulence, but presumably the result of local turbulence generation at the base of the pycnocline. It is important to note that dissipation measurements are very difficult, especially in the strongly stratified and potentially sheared environment of the pycnocline base. The presented values of ϵ should therefore not be treated as ground truth. However, the dissipation peak at the base of the pycnocline appears to be a robust result.

The vertical position of the SCM is just above the dissipation maximum (compare Figures 4b and 4c). This indicates that the turbulence generated here is the main driver of nutrient flux from the bottom layer into the base of the pycnocline and thus the major fuel pump for the SCM. Therefore, exploring the processes behind this turbulence maximum at the base of the pycnocline will be our primary focus.

Table 1
Model Setup Configurations

setup	Realistic	No meteo	Just meteo	M_2 only	Anticyclonic	Cyclonic
Abbr.	R	RnM	Met	M2	ACy	Cy
Current forcing	ADCP	ADCP	No	Harm. M2	M2 anticy.	M2 cyclonic
Surface fluxes	Yes	No	Yes	No	No	No

3. Model

In order to study the mechanisms and forcing agents behind the turbulence maximum at the base of the pycnocline, we employ a state-of-the-art one-dimensional turbulence closure model. This allows for a detailed analysis of the turbulence generation at the base of the pycnocline as well as full control over the external forcing involved. We will also use the model to investigate the ability of the turbulence at the base of the pycnocline to effectively flux tracers (e.g., nutrients) from the bottom layer into the stratified pycnocline, the habitat of the SCM.

3.1. The General Ocean Turbulence Model

As a one-dimensional water column model, we apply the General Ocean Turbulence Model (GOTM, Burchard & Bolding, 2001; Umlauf & Burchard, 2005; Li et al., 2021, see also www.gotm.net) which includes budget equations for momentum and tracers. All horizontal gradients are either ignored (assuming horizontal homogeneity) or prescribed (such as horizontal pressure gradients). Surface momentum and buoyancy fluxes are calculated from meteorological data through bulk formulae (Fairall et al., 2003). At the bottom boundary, vertical fluxes of momentum are based on the assumptions of no-slip boundary conditions and the existence of a logarithmic layer directly above the bottom. The vertical turbulent fluxes of momentum and tracers in the water column are parameterized utilizing two-equation turbulence closure models with algebraic second moments. One turbulence budget equation is for the turbulent kinetic energy per unit mass (TKE). The other equation parameterizes the budget of a length-scale-related quantity such as the turbulent dissipation rate per unit mass, ϵ . The buoyancy term in the length-scale-related equation is calibrated in a way that a steady-state gradient Richardson number of $Ri_g^{\text{st}} = 0.25$ is reproduced in homogeneous shear layers (Burchard & Baumert, 1995; Umlauf & Burchard, 2005). This is consistent with a mixing efficiency of $\Gamma = 0.2$ (Burchard & Hetland, 2010; Umlauf, 2009), a value that has been proposed by Osborn (1980) for such situations.

3.2. Simulation Versus Observations

In a first step, we use a realistic setup of the model to see how well it compares to our observations. To this end, we use realistic surface fluxes (Cosmo–Reanalyse, Kaspar et al., 2020) as well as depth-averaged current velocities measured by the bottom-mounted ADCP to force the model. This method applies the tidal forcing by oscillating surface elevation gradients in a way that the observed vertically averaged current velocity is reproduced (Burchard, 1999). The model is initialized with the measured temperature and salinity profiles displayed in Figure 4a. In the following, we call this particular model configuration “setup R” (see Table 1).

While the general density structure is comparable between model and observations, it is worth noting a number of differences (Figures 5a and 5b). In the observations, we see substantial density variability in the surface layer as well as a general tendency of decreasing density leading up to the strong wind event on day 221. The model does not sufficiently capture either of these characteristics. Furthermore, we note that vertical mixing during the strong wind event is underrepresented in the model indicated by a weaker density contrast between upper and lower layer in the observations than in the model following day 221. A possible explanation for these discrepancies is the likely slightly inaccurately modeled surface fluxes, or lateral density gradients, which are not represented in the model. Another noticeable difference is a slightly sharper density gradient at the base of the pycnocline in the simulations compared to the observations, which is likely due to a missing internal wave parameterization in the model.

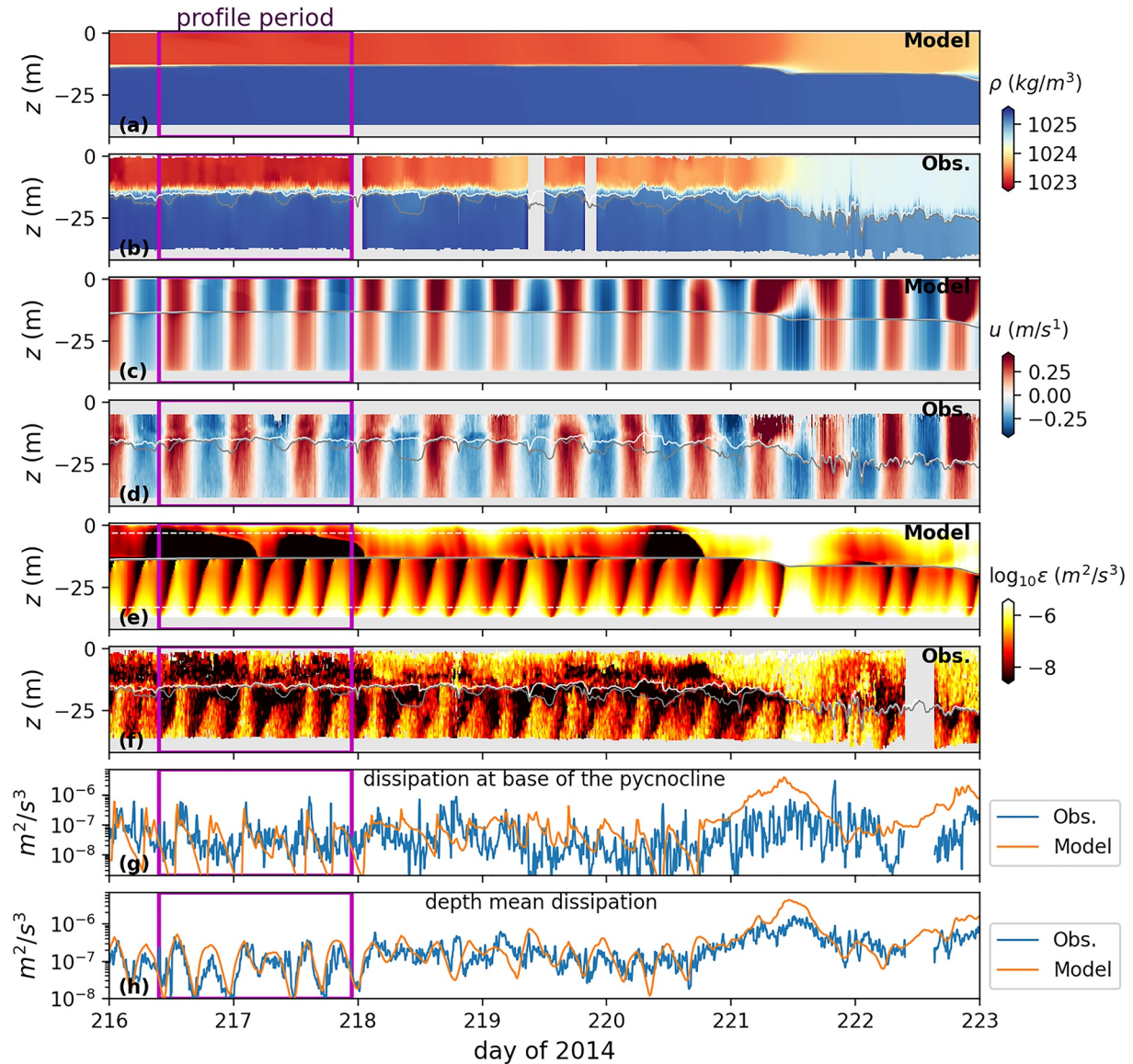


Figure 5. Comparison between observations and model simulations (setup: R): (a and b) density; (c and d) eastward component of velocity; (e and f) dissipation of turbulent kinetic energy; (g) dissipation rate at the base of the pycnocline (PCB) (vertically averaged ± 2 m around the 80% criteria); and (h) depth-averaged dissipation rate, where observations are in blue and model results in orange. Since the glider does not provide reliable dissipation estimates close to the surface and bottom, we excluded the top and bottom 3 m of the water column from the depth average, indicated by dashed white lines in panel (e). Gray line in (a–f) marks the 90% and white line the 80% criteria for the position of the PCB.

It is not surprising that the model can reproduce the observations in terms of general strength and direction of velocity, since it is directly forced by the observed depth-averaged current velocity (Figures 5c and 5d). However, the model is able to capture most of the vertical current structure, which is not prescribed, in particular significant shear across the base of the pycnocline (white line in Figures 5c and 5d). Some disagreement in the strength of the near-surface velocities around days 218–219, may be due to discrepancies between simulated and actual wind stresses, the latter of which have not been measured directly.

In terms of the turbulence dissipation rate (Figures 5e and 5f), most features present in the observations are well-captured in the model. One noticeable difference can be seen in the bottom layer, where we find an asymmetry between ebb and flood dissipation patterns (Figure 5f), which are not apparent in the model (Figure 5e). This asymmetry in dissipation seems to be linked to a weak periodic restratification of the bottom layer, indicated by the periodic vertical migration of the 90% relative to the 80% condition for the base of the pycnocline (compare

gray and white lines in Figure 5f). When averaged over several tidal cycles, this behavior yields an apparent separation of the mean position of the 80% and 90% definition of the pycnocline base in the observations (Figure 4), which does not exist in the model simulations.

The weak periodic stratification of the BML seems to suppress vertical growth of bottom-generated turbulence, indicated by the fact that the 90% threshold for the base of the pycnocline seems to act as an effective lid for bottom-generated turbulence (gray line in Figure 5f). A possible explanation for this periodic stratification is the horizontal density gradients that are differentially advected by tidal currents in a process called *tidal straining* (Simpson et al., 1990), which can be reproduced with GOTM, when horizontal gradients of temperature and salinity are prescribed (Simpson et al., 2002). This hypothesis is supported by the fact that the weak stratification seemingly reoccurs in phase with the tidal currents. Since the model does not consider horizontal gradients, it cannot reproduce this behavior. It is worth noting in this context that the mid-water column dissipation maximum remains at the main pycnocline, indicated by the 80% threshold (white line), even during times of weak bottom layer stratification (compare the gray and white lines in Figure 5f).

The overall agreement between the model and observations in terms of turbulence dissipation is surprisingly good, given the simplicity of the model. This is true on a qualitative level (compare the patterns in Figures 5e and 5f) but also in a quantitative sense. The dissipation at the base of the pycnocline (averaged over ± 2 m around the white line in Figures 5e and 5f), agrees well between the model and observations (Figure 5g). The depth-averaged dissipation rates also compare well between model and observations (Figure 5h). Note that we excluded the top and bottom 3 m of the water column from the average (white dashed lines in Figure 5e) to mimic the observational limitations imposed by the glider flight.

In summary, we find that the model is able to reproduce most of the turbulence features as well as the vertical current structure found in the observations. This gives us confidence that we can use the model to explore the turbulence characteristics at the base of the pycnocline, which is the primary focus of this study.

3.3. Setup Configurations

A major goal of our study is to disentangle the influence of the different forcing agents and evaluate their relative importance for turbulence production at the base of the pycnocline, which is likely important to provide the necessary nutrient fluxes to fuel the SCM. To this end, we construct different model setups (Table 1):

- R : realistic current and surface forcing;
- RnM: realistic current forcing but no surface fluxes;
- Met: no current forcing but realistic surface fluxes;
- M2: only M_2 -tidal forcing;
- ACy: only anticyclonic M_2 forcing;
- Cy: only cyclonic M_2 forcing.

All setups are initialized with temperature and salinity profiles from the observations as displayed in Figure 4a. The most realistic setup (R) is driven by full meteorological fluxes provided by a reanalysis product (Cosmo–Reanalyse, Kaspar et al., 2020) and by prescribed depth-averaged velocities measured by the bottom-mounted ADCP. To study the influence of surface forcing in general, and wind in particular, we construct the setups RnM and Met. Setup RnM has full current forcing, but no meteorological surface fluxes. In contrast, Met has only realistic surface fluxes but no current forcing. To study the influence of tides and their individual components, we use four different setups with increasingly idealized tidal forcing (RnM, M2, Cy, ACy). All four setups have no surface fluxes prescribed. RnM uses the observed depth-averaged velocities as forcing, containing several other sources of high- and low-frequency variability besides different components of the tide. Setup M2 is forced solely by the M_2 -component of the tide, which we obtain by harmonic analysis of the depth-averaged ADCP signal. In a further step of abstraction, we are interested in the influence of the polarity of the tidal signal. To this end, we construct an artificial tidal signal containing a purely anticyclonic (cyclonic) tidal current ellipse to force setup ACy (Cy). To ensure comparability between different setups, we choose the amplitude of the artificial tidal forcing for ACy and Cy such that the tidally averaged kinetic energy of the depth-averaged velocity is the same as for setup M2 (Table 2). The simulation results of the different setups are compared in Figure 6.

Table 2

Time Averages of Different Quantities For All Model Setups: (Third Column) Depth of the Base of the Pycnocline (90% Criterion); (Fourth Column) Time ($\langle \rangle$) and Depth ($\langle \rangle_z$) Kinetic Energy of the Barotropic Currents $\langle E_{BT} \rangle = \langle \langle U \rangle_z^2 \rangle$, With $U = u + iv$; and (Fifth Column) Kinetic Energy in the Velocity Anomaly $\langle E_a \rangle = \langle \langle (U - \langle U \rangle_z)^2 \rangle_z \rangle$

setup	Abbr.	z @ PCB		
		M	$\langle E_{BT} \rangle$ $10^{-4} \text{ m}^2 \text{ s}^{-2}$	$\langle E_a \rangle$ $10^{-4} \text{ m}^2 \text{ s}^{-2}$
Realistic	R	-13.6	600.0	54.3
No meteo	RnM	-13.6	600.0	44.2
Just meteo	Met	-17.6	1.4	3.7
M_2 only	M2	-14.0	568.0	60.1
Anticyclonic	ACy	-13.4	568.0	86.1
Cyclonic	Cy	-15.3	568.0	6.2

4. Turbulence at the Base of the Pycnocline

This section will evaluate the transport equation for turbulent kinetic energy at the base of the pycnocline for different model simulations. Based on the realistic simulation, we will demonstrate that the observed peak in dissipation at the base of the pycnocline is not caused by vertical transport of bottom-generated turbulence but local shear production. By comparing different model setups, we can show that surface fluxes, including wind, have little to no influence on turbulence generation at the base of the pycnocline during calm weather. Instead, we find that most of the turbulence is driven by tidal currents, in particular the M_2 tidal constituent. Furthermore, we will demonstrate that besides the strength of the M_2 tide, its polarity is also critical for turbulence production at the base of the pycnocline.

4.1. Turbulent Kinetic Energy

The transport equation for turbulent kinetic energy applied here can be written as

$$\partial_t k = T_k + P + B - \epsilon \quad (1)$$

where ∂_t indicates a partial derivative with respect to time, T_k is the summation of all possible vertical transport terms, P is the shear production, and B is the buoyancy production. In the one-dimensional model all horizontal

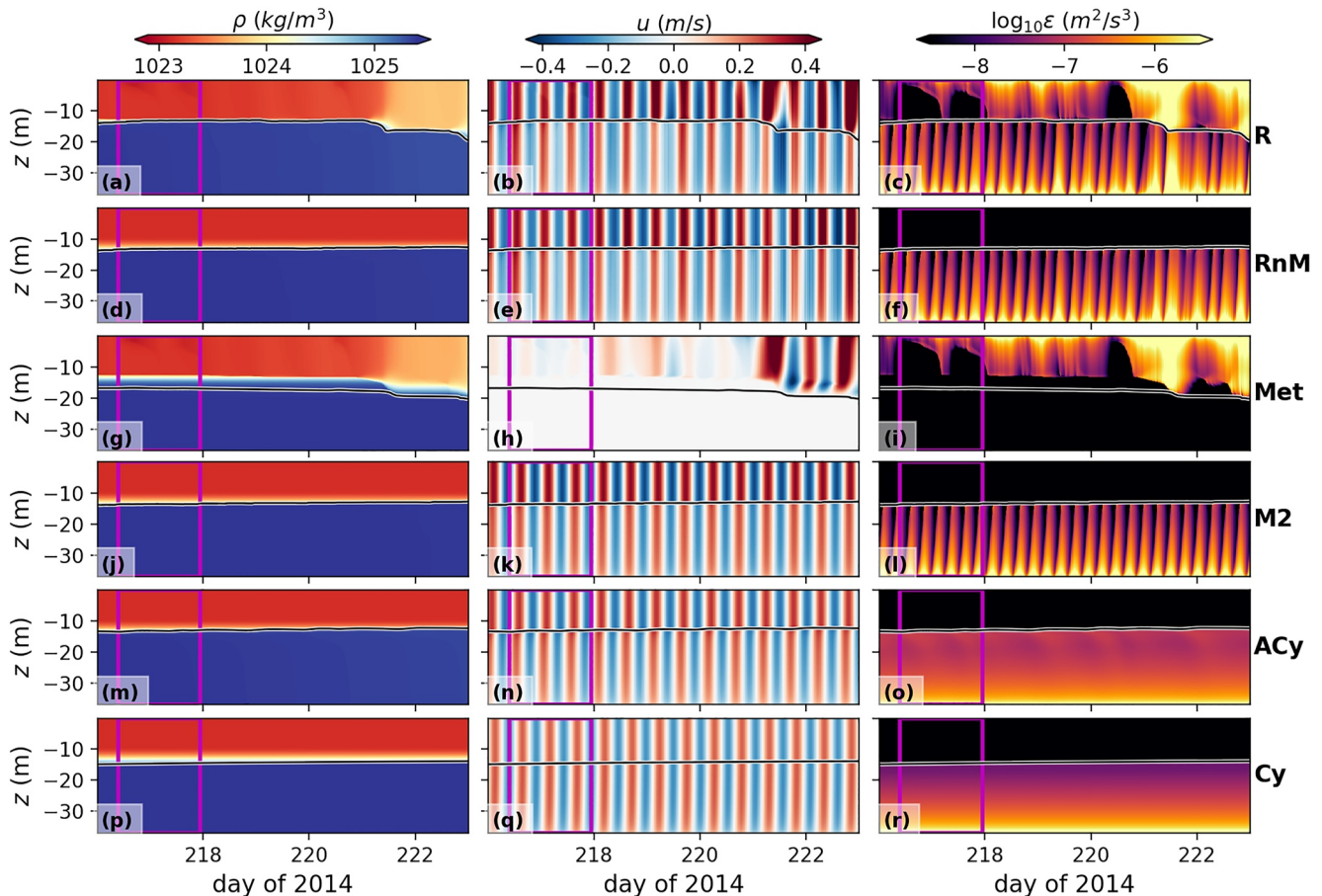


Figure 6. Comparison between different model setups, where each row corresponds to a different setup (Table 1): (left) density, (middle) eastward component of velocity, and (right) dissipation of turbulent kinetic energy. Gray lines indicate the location of the base of the pycnocline (90% criterion).

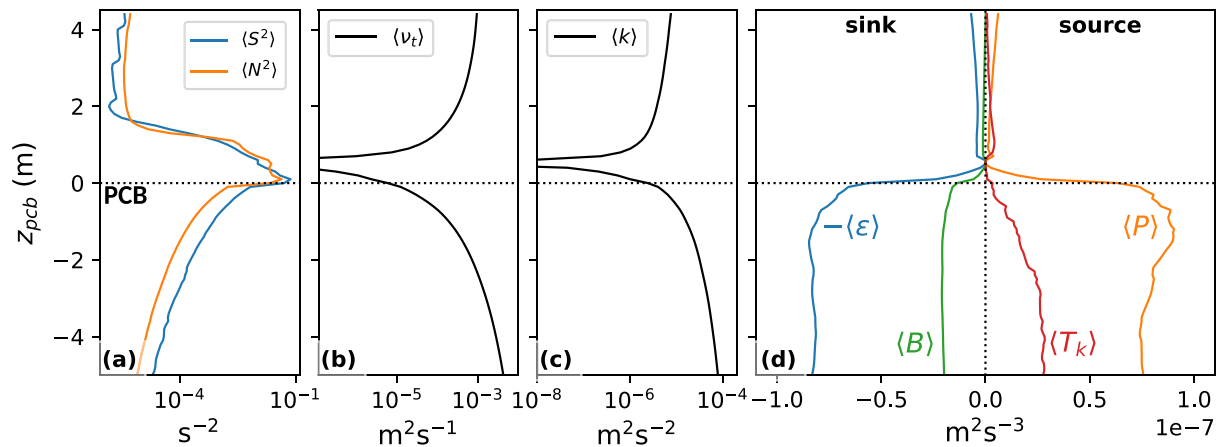


Figure 7. Profiles of different contributions to the turbulent kinetic energy per unit mass (TKE) balance for model setup R, centered around the base of the pycnocline ($z_{pcb} = 0$, 90% criterion), averaged in time (magenta box in Figure 6a): (a) shear squared (blue) and Brunt-Väisälä frequency squared (orange); (b) turbulent viscosity; (c) turbulent kinetic energy; (d) dissipation of TKE (blue), shear production (orange), buoyancy production (green), and vertical turbulent transport (red).

gradients of mean quantities are ignored and the vertical turbulent fluxes are modeled with a down-gradient assumption, which yields the following expressions for the individual terms in Equation 1:

$$T_k = \partial_z (\nu_t \partial_z k) \quad (2)$$

where ∂_z denotes the partial derivative with respect to z and ν_t the turbulent viscosity;

$$P = \nu_t S^2 \quad (3)$$

where $S^2 = (\partial_z u)^2 + (\partial_z v)^2$; and

$$B = -K_p N^2 \quad (4)$$

with the turbulent diffusivity K_p and Brunt-Väisälä frequency squared $N^2 = -(g/\rho_0)\partial_z \rho$, where $g = 9.81 \text{ m s}^{-2}$ and $\rho_0 = 1,025 \text{ kg m}^{-3}$ are gravitational acceleration and reference density, respectively.

4.2. Realistic Simulation

We evaluate the different terms of Equation 1 at the base of the pycnocline. To this end, we construct a vertical coordinate, z_{pcb} , that is centered around the instantaneous position of the base of the pycnocline (90% criterion). Following this coordinate system, we average in time over three consecutive M_2 tidal cycles (see magenta box in Figure 6) to gain the profiles displayed in Figure 7. This averaging procedure is indicated by the $\langle \cdot \rangle$ braces.

The profile of $\langle N^2 \rangle$ shows a high stratification region approximately in the range $0 < z_{pcb} < 2 \text{ m}$, with a maximum of $\langle N^2 \rangle > 10^{-2} \text{ s}^{-2}$ just above $z_{pcb} = 0$, the vertical location of the base of the pycnocline (Figure 7a, orange line). Just below the maximum in $\langle N^2 \rangle$, we find a maximum in $\langle S^2 \rangle$ at the base of the pycnocline (Figure 7a, blue line).

As in the observations, we find a maximum of dissipation ($\langle \epsilon \rangle$) in simulation R close to the base of the pycnocline (compare blue line in Figure 7d with Figure 4c). Although the maximum in the simulation is less pronounced than in the observations, their magnitude is comparable, agreeing to within a factor of two. However, something we cannot investigate based on the observations becomes obvious in the simulation results: the maximum in dissipation is accompanied by a comparable peak with the opposite sign in local shear production (compare blue and orange lines in Figure 7d).

Vertical transport of bottom-generated turbulence is relevant in the deeper bottom mixed layer ($z_{pcb} < -2 \text{ m}$), but close to the base of the pycnocline local shear production ($\langle P \rangle$) is a much stronger source for k than $\langle T_k \rangle$ (red line, Figure 7d). In fact, $\langle T_k \rangle$ tends toward zero at $z_{pcb} = 0$. The mirroring profiles of $\langle P \rangle$ and $\langle \epsilon \rangle$ and the vanishing $\langle T_k \rangle$ term indicated that the dissipation peak at the base of the pycnocline is not due to vertical transport of bottom-generated turbulence, but in fact caused by local shear production.

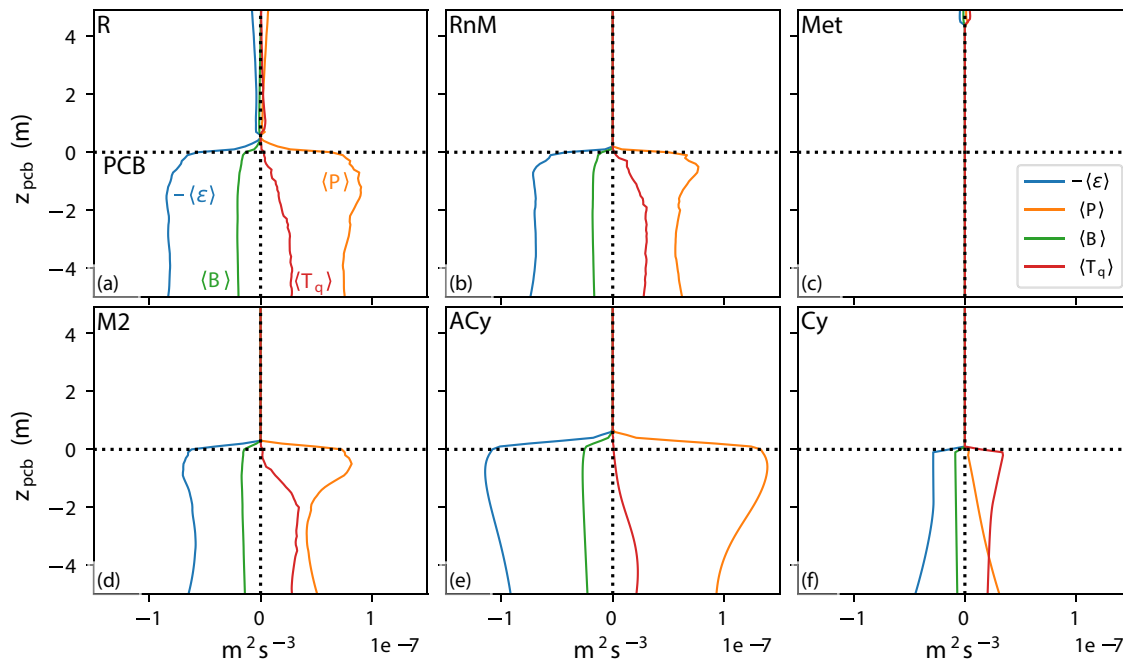


Figure 8. Same as Figure 7(d) comparing all model setups.

It is important to note that the profiles in Figure 7 correspond to a relatively calm period in terms of wind forcing. During stronger wind events, the TKE source terms above the pycnocline can be as strong or even stronger than below the pycnocline (Figure 6c).

Buoyancy production ($\langle B \rangle$) inside and at the base of the pycnocline is $\approx 20\%$ of $\langle \epsilon \rangle$, that is, the mixing efficiency is $\Gamma \approx 0.2$ (see Section 3.1) indicating efficient mixing in this region. Further below, in the bottom mixed layer, the efficiency decreases.

4.3. Tides Versus Wind

We begin our analysis by evaluating the importance of surface fluxes, wind in particular, for turbulence production at the base of the pycnocline. To this end, we compare setup *R* to RnM, which are identical in terms of velocity forcing, but RnM has zero surface fluxes. Above the pycnocline ($z_{pcb} > 1$ m) some deviation can be seen, where we practically find no source of TKE in RnM (Figure 8b) as opposed to weak production and vertical transport in *R* (Figure 8a). However, below $z_{pcb} < 1$ m, the different TKE terms in simulation RnM are very similar to those of setup *R* both in terms of magnitude and qualitative behavior. In contrast, simulation Met, the setup with surface forcing only, shows practically no turbulence activity at the base of the pycnocline (Figure 8c), indicated by all TKE terms being close to zero below $z_{pcb} = 1$ m. This suggests that surface fluxes have little to no influence on the turbulence production at the base of the pycnocline.

After establishing that current forcing drives almost all turbulence at the base of the pycnocline during calm weather, we would like to investigate how much of this can be accounted for by the main tidal constituent, the M_2 tide, alone. To this end, we compare setup M2 to RnM (Figures 8b and 8d). Besides some minor differences in the vertical structure of the TKE terms, both setups compare very well in terms of turbulence at the base of the pycnocline. This suggests that the M_2 tide is the main driver for turbulence at the base of the pycnocline.

Now we will demonstrate that not just the amplitude of the M_2 tide is key to turbulence production at the base of the pycnocline, but also the polarity of the tide, that is, the relative strength of its anticyclonic and cyclonic component.

To this end, we compare setups ACy and Cy to M2. All three setups have identical mean barotropic energy $\langle E_{BT} \rangle$, however, significantly different kinetic energy levels in the velocity anomaly, $\langle E_a \rangle$ (Table 2). While setup

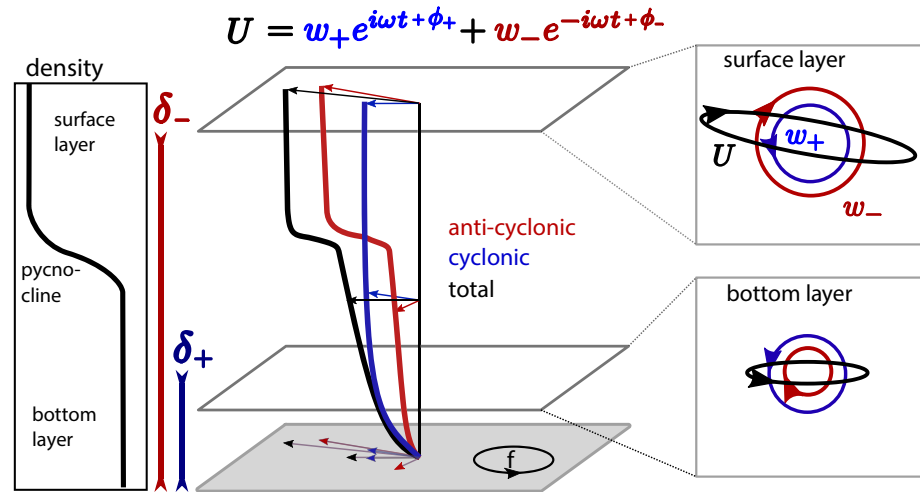


Figure 9. Conceptual sketch of the decomposition of the tidal currents into cyclonic (blue) and anticyclonic (red) components each with different boundary layer thicknesses (δ_+ , δ_-). Since δ_- reaches beyond the height of the pycnocline and δ_+ does not (see left panel), the anticyclonic component is strongly sheared at the base of the pycnocline, whereas the cyclonic component is not. This results in a different composition (polarity) between the surface and bottom layers as indicated on the right.

ACy has even more kinetic energy in the velocity anomaly than setup M2, setup Cy has only about 10% of $\langle E_a \rangle$ compared to M2. This suggests that the anticyclonic component of the tide yields significantly more internal shear than the cyclonic component, which is also reflected in the TKE production terms (Figures 8d–8f). While ACy shows the strongest TKE production of all setups, Cy has only little dissipation and hardly any local shear production at the base of the pycnocline. It is the only setup where vertical transport of bottom-generated TKE outweighs local production at the base of the pycnocline, which implies that detrainment probably dominates over entrainment into the pycnocline for setup Cy. This demonstrates that the polarity of the tidal signal is critical for the vertical structure and strength of turbulence at the base of the pycnocline.

5. Tidal Polarity

In this section, we explore the role of tidal polarity in the turbulence production at the base of the pycnocline, providing some background and possible explanation for the profound differences between model setup ACy and Cy described in the previous section.

The depth-averaged tidal velocities vector is periodically rotating in the horizontal plane, describing the so-called *tidal ellipse* over a full rotation. Since a vector in the horizontal plane only has two components, it can be expressed as a complex number ($U = u + iv$), where the real part (u) corresponds to the eastward and the imaginary part (v) to the northward velocity component. Any complex periodic function (e.g., the tidal velocity vector in the horizontal plane), can be decomposed into a superposition of anticyclonic and cyclonic rotating components, each with its own radius and frequency. The M_2 -tidal velocity ellipse may be written as

$$U_{m2}(t) = w_+ e^{i\omega_{m2}t + \phi_+} + w_- e^{-i\omega_{m2}t + \phi_-} \quad (5)$$

where ω_{m2} denotes the M_2 -tidal frequency, w_+ and w_- the amplitudes and ϕ_+ and ϕ_- the phases of the cyclonic and anticyclonic component, respectively (Figure 9).

The decomposition Equation 5 exposes an asymmetry in the tidal dynamics that arises from Earth's rotation, which is cyclonic that is counterclockwise in the Northern and clockwise in the Southern Hemisphere. Depending on geographic location, one of the two terms in Equation 5 is moving with and one against Earth's rotation.

This asymmetry becomes important once friction is taken into account. Prandle (1982) provides analytical solutions for the bottom Ekman layer thickness, that is, the layer in which the velocity direction and strength is influenced by bottom friction, for the idealized case of constant viscosity ($\nu_t = \text{const}$) and no vertical stratification

($N^2 = 0$), $\delta_+ = \sqrt{v_t/(\omega + f)}$ and $\delta_- = \sqrt{v_t/(\omega - f)}$, with the Coriolis frequency $f = 2\Omega \sin \phi$, where Ω denotes the rotation rate of the Earth and ϕ the latitude.

We can calculate the ratio between the anticyclonic and cyclonic Ekman layer thickness for the M_2 tidal component ($\omega_{m2} = 1.41 \cdot 10^{-4} \text{ s}^{-1}$) at the latitude of the field site ($\phi = 54.5^\circ\text{N}$, $f = 1.19 \cdot 10^{-4} \text{ s}^{-1}$), $\delta_-/\delta_+ = [(\omega_{m2} + f)/(\omega_{m2} - f)]^{1/2} = 3.45$. This ratio implies that shear stress from bottom friction of the anticyclonic component penetrates substantially higher up into the water column than for the cyclonic component (Figure 9).

Simpson and Tinker (2009) demonstrated that different tidal polarities can yield very different bulk-mixing efficiencies for bottom-generated turbulence from tides, simply because the turbulent bottom boundary layer penetrates further up into the water column toward regions of stronger stratification if the tide is primarily anticyclonically polarized.

At the pycnocline, vertical turbulent transport of momentum is inhibited due to stratification. This means that tidal stresses generated at the bottom do not affect the water above the pycnocline, which can yield a situation where the tidal currents above the pycnocline are at their free stream velocity, whereas below they are substantially decelerated by bottom friction. We have already established that there is a dramatic difference in the frictional boundary layer thickness of the anticyclonic and cyclonic tidal component in midlatitude regions. Therefore, the cyclonic component can reach its free stream velocity already below the pycnocline, resulting in no shear across the pycnocline, whereas the anticyclonic component is strongly sheared across the pycnocline (Figure 9). Souza and Simpson (1996) describe, for instance, a situation where the polarity of the tidal currents changes across the pycnocline from being approximately equal ($w_- \approx w_+$) below, to primarily anticyclonic ($w_- > w_+$) above the pycnocline. This means that tidal shear across the pycnocline is primarily anticyclonically polarized (Maas & van Haren, 1987; van Haren, 2000).

This phenomenon can also be observed in our simulation where we find substantial shear across the pycnocline for setup ACy and practically no shear for setup Cy (compare Figures 6n and 6q). From a turbulence perspective, strong shear at the base of the pycnocline in setup ACy is associated with strong turbulence production (orange line Figure 8e). On the contrary, weak shear, found in setup Cy, yields no significant turbulence production at the base of the pycnocline, instead vertical transport of bottom-generated turbulence dominates (red line Figure 8f). The issue with vertically transported turbulence from the bottom is that it mainly yields detrainment (entrainment from pycnocline waters into the BML, for a sketch see Figure 2). Hence, it is not suitable to flux nutrients into the base of the pycnocline. In contrast, direct shear instabilities at the base of the pycnocline, as indicated by a local maximum in P for setup ACy (Figure 8e), can entrain water from the BML into the stratified base of the pycnocline, and therefore are potentially suitable to provide nutrients for the SCM.

Tidal shear is specifically focused at the base of the pycnocline, since it grows from below, having its origin at the bed. If stratification at the base of the pycnocline is strong enough to inhibit most of the vertical momentum transport, the tidal currents will already be close to free stream right above the base of the pycnocline, which in turn means that tidal shear will have a local maximum right at the base of the pycnocline, which is consistent with our observations (Figure 7a). Since tidal shear is focused at the base of the pycnocline, its associated turbulence production is especially suitable to entrain BML water into the lower pycnocline and therefore to fuel the SCM (see Section 6).

In summary, we find that tidal shear is the main source for TKE at the base of the pycnocline, where the anticyclonic component of the tides provides the overwhelming contribution. This suggests that besides the sole magnitude of the tidal currents, the polarity is critical to provide favorable conditions for turbulence at the base of the pycnocline, which is able to fuel the SCM.

6. Diapycnal Transport

In this section, we will explore the ability of the different model setups to entrain a passive tracer from the BML into the stratified pycnocline. The tracer is meant to mimic some of the distribution characteristics of nutrients, but could also represent other water constituents. To this end, we consider typical stratified summer conditions, where we find abundant nutrients in the BML and nutrient deficiency in the surface layer and pycnocline region, respectively.

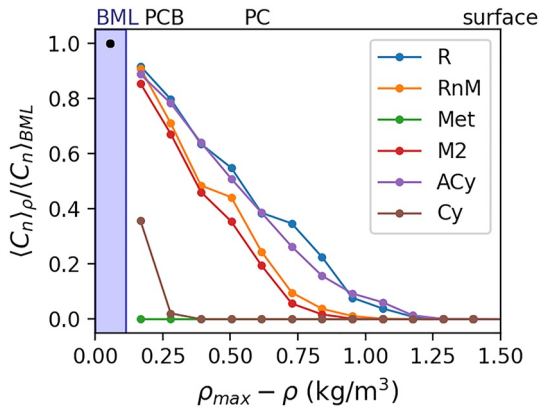


Figure 10. Tracer concentration in density space. Tracer concentration collected in density bins (relative to well-mixed bottom layer (BML) density) and averaged in time over the profile period. x -axis shows the density difference with respect to the BML density, such that the left side corresponds to the BML and the surface layer extends to the right. Since the pycnocline contains per definition 90% of all density variation, this resolves the pycnocline, where smaller values of $\rho_{max} - \rho$ correspond to the base of the pycnocline (PCB). All concentrations are normalized by their respective well-mixed bottom layer (BML) concentration. Colors indicate different setups as listed in the legend.

The passive tracer, c_n , is initialized in the simulations with an arbitrary non-zero concentration below $z = -25$ m and zero elsewhere. During the initial spin-up phase of the simulation, the tracer evenly spreads within the BML. The goal is to start each simulation after spin-up with a vertical profile of c_n , where we find an approximately constant concentration in the BML and zero everywhere else. A close to even distribution of c_n below the base of the pycnocline is achieved within 24 hr after the start of the simulation. For our following analysis, we concentrate on the profile period (magenta lines in Figure 6), which starts more than 5 days after the start of the simulation, and therefore, should provide plenty of spin up time.

The distribution of tracer is used to gauge how effective the different model scenarios are in fluxing water constituents (e.g., nutrients) from the BML into the stratified pycnocline. To visualize this, it is helpful to look at the water column in density space, since it reflects the time-integrated diapycnal transport into the pycnocline. In Figure 10, we collect all c_n values during the profile period in density bins, average, and then normalize by the BML average ($\langle c_n \rangle_{BML}$). Density bins ($\rho_{max} - \rho$) are constructed such that the entire BML falls into the first bin (blue shading Figure 10). With increasing $\rho_{max} - \rho$, we move upward through the pycnocline, where smaller values correspond to the base of the pycnocline. The surface layer is at $\rho_{max} - \rho \approx 2.5$ kg m⁻³ and has negligible tracer concentration.

The realistic scenario R facilitates substantial tracer flux into the base of the pycnocline, with a close to linear decrease of $\langle c_n \rangle$ in density space (blue line, Figure 10). $\langle c_n \rangle$ is larger than 50% of the BML value across many density bins. If the tracer is interpreted as nutrients, this could potentially yield sufficient food supply for an SCM at the base of the pycnocline in setup R . Also setup RnM , $M2$, and ACy appear to provide comparable tracer fluxes into the pycnocline. Setup Met and Cy , on the other hand, result in only very little to no diapycnal flux into the stratified pycnocline.

The tracer distribution between setup R and RnM is comparable, with slightly less $\langle c_n \rangle$ values for RnM compared to R (compare orange and blue lines Figure 10). The slight difference between the two scenarios hints toward some minor effect of surface forcing on the diapycnal flux at the base of the pycnocline. However, surface forcing alone (setup Met , green line) is not able to generate any detectable fluxes. This indicates that the difference between R and RnM in tracer flux from the BML into the base of the pycnocline is due to a nonlinear interaction of depth-averaged current and wind forcing inside the pycnocline. The diapycnal flux in setup $M2$ is only marginally reduced compared to RnM (compare red and orange lines in Figure 10), suggesting that the majority of tracer supply in the pycnocline is associated with the M_2 tidal component.

Consistent with our considerations in the previous section in the context of turbulence production at the base of the pycnocline, we find that the polarity of the M_2 tide is key. ACy generates tracer fluxes, which are comparable to setup R and even larger than those of setup $M2$ and RnM . On the other hand, setup Cy generates hardly any tracer flux into the base of the pycnocline.

If we naively interpret the passive tracer as nutrients, we find that diapycnal fluxes from the BML into the base of the pycnocline could potentially be sufficient to fuel the SCM for all but two (Met and Cy) of the scenarios considered here. We find that the largest fraction of this flux is associated with the M_2 tidal forcing, with a minor secondary contribution from surface forcing. The polarity of the M_2 tidal currents is crucial, where the anticyclonic component dominates the diapycnal flux into the base of the pycnocline.

It is important to note that real nutrients are not passive tracers, since they can be consumed and/or generated in the water column by remineralization. Therefore, one needs to be careful when interpreting our passive tracer as nutrients. To fully understand the intricate balance between diapycnal nutrient transport and SCM growth, it would be necessary to employ a more sophisticated biogeochemical model with realistic nutrient concentrations. Nevertheless, our results indicate that the diapycnal transport that fluxes nutrients from the BML into the pycnocline is largely governed by the M_2 tide.

7. Discussion

In this section, we discuss several forcing mechanisms and dynamical processes to gauge their ability to support diapycnal fluxes into the base of the pycnocline to potentially fuel the SCM under calm summer conditions.

7.1. Detrainment Versus Entrainment

When studying turbulent fluxes in and out of the pycnocline, it is crucial to consider where the turbulence that produces these fluxes originates. If turbulence is solely generated in the BML, it can only act on the pycnocline from below. However, this will yield detrainment out of the pycnocline, by which we mean entrainment of less dense pycnocline waters into the BML. Such detrainment will tend to decrease the BML density but also to sharpen the base of the pycnocline in terms of stratification, since it erodes the densest part of the pycnocline. Detrainment of the pycnocline is not able to flux any nutrients from the BML into the stratified pycnocline. It can even be harmful to the SCM by eroding it from below, submerging its phytoplankton into the deeper and darker BML (Hopkins et al., 2021; Sharples, 2007). Indications for such pycnocline detrainment events can be observed on a regular basis, for instance, the sudden chlorophyll-*a* increase in the BML end of day 220 in Figure 3c.

In order to fuel the SCM, it is necessary to entrain fluid from the nutrient-rich BML into the stratified pycnocline; the habitat of the SCM. The effect of entrainment will be a widening of the pycnocline and consequently a decrease of stratification at the base of the pycnocline. Since entrainment mixes nutrient rich BML water into the base of the pycnocline, it works as the fuel pump for the SCM. Entrainment into the base of the pycnocline (the opposite of detrainment) can only be accomplished by turbulence that originates directly within the pycnocline. Therefore, the most likely source for entrainment of BML waters into the pycnocline is shear instabilities inside the base of the pycnocline.

In most real-world situations, the base of the pycnocline and hence the SCM will be governed by an intricate balance between detrainment and entrainment, which can easily be shifted toward one or the other by changes in forcing, for example, wind events, passing internal wave trains, or the spring-neap cycle. Sharples (2007) finds that the neap-spring cycle can modulate alternating periods of detrainment and entrainment. However, when considering the effect of the barotropic tide in isolation, it is not obvious how the diapycnal flux at the base of the pycnocline changes in response to an increased tidal amplitude during spring tide. On the one hand, higher levels of bottom-generated turbulence may yield increased pycnocline erosion from below. On the other hand, elevated shear at the base of the pycnocline yields stronger local shear production of turbulence, and hence increased entrainment. Which of the two effects dominates at a given location will likely depend on a multitude of factors.

7.2. Internal Waves

We already established that instabilities inside the pycnocline are key to generating turbulence that can entrain nutrients from the BML into the stratified pycnocline water. It is believed that internal waves are one of the most important processes to generate instabilities in the otherwise stably stratified interior of the ocean (Ferrari & Wunsch, 2009). Also in shelf regions as internal waves shoal, they can give rise to strong shear instabilities in the interface (MacKinnon & Gregg, 2003; Moum et al., 2003). Becherer et al. (2021a, 2021b) demonstrated that the energy flux divergence of the internal tide can explain a significant fraction of the observed dissipation in many inner shelf seas around the world. In these regions, the mixing caused by the internal tide is likely a leading source for a diapycnal flux of nutrients (Sharples, Moore, & Abraham, 2001).

It is impossible to assess the role of internal waves based on the one-dimensional water-column model used here. By deploying a similar model, Simpson et al. (1996) found an inability of the simulations to capture a large fraction of turbulence observed inside the pycnocline indicating a leading role of internal waves in pycnocline mixing at their measurement location.

A common way to account for the missing contribution of high-frequency internal waves in these models is to prescribe a background TKE (Burchard et al., 2002). This effectively provides some mixing in regions, where the mean shear is not strong enough to overcome the stabilizing effect of stratification. Such a crude way of parameterizing the effect of high-frequency internal waves does not try to replicate any of the involved mechanisms.

Consequently, one-dimensional turbulence closure models like the one utilized for this study are not a suitable tool to estimate the internal wave contribution to overall mixing.

In light of this major flaw of our model, it is surprising that we can capture most of the dissipation features seen in the observations including a substantial diapycnal flux from the BML into the base of the pycnocline. This suggests that at least in tidally dominated systems like the North Sea, other processes, for example, direct tidal forcing and wind, are accounting for a large fraction of the observed mixing. In this context, it is important to note that internal wave energy at our site, as estimated from the isopycnal displacement at the pycnocline (usually below 1 m, not shown), is more than one order of magnitude smaller than the kinetic energy associated with the shear of the barotropic tide ($\langle E_a \rangle$). This suggests only a minor role for both low-frequency internal tides and high-frequency internal waves at our site.

7.3. Wind Forcing

We demonstrated here that the wind has little influence on turbulence production at the base of the pycnocline during calm summer conditions and hence on the nutrient fluxes from the BML into the pycnocline. A reason for this is that wind generates stress at the surface of the ocean, which propagates downward through the surface mixed layer, resulting in noticeable shear at the top of the pycnocline. Any associated turbulence will first and foremost affect the upper pycnocline and not as much the lower base of the pycnocline. Hence weak to moderate direct wind forcing is not feasible to provide nutrient fluxes from BML into the base of the pycnocline for fueling the SCM.

However, strong wind events can generate turbulence that is able to penetrate all the way through the pycnocline. This can result in nutrient fluxes from the BML across the entire pycnocline even into the surface mixed layer. Such an event can be seen in our observations, where we find a significant increase in chlorophyll-a concentration in the surface layer following the strong wind event on day 221 (Figure 3c). These wind events can entirely mix the water column thereby ending the stratified summer season in these systems (Schultze et al., 2020). However, well-mixed conditions come with vertically homogeneous phytoplankton distributions, where no clear SCM can be identified anymore. The missing stratification and the absence of an SCM dramatically changes the dynamics of the system with strong implications for the shelf as a carbon pump (Thomas et al., 2004).

By generating inertial oscillations, even weaker wind events can indirectly influence turbulence production inside the pycnocline. Inertial oscillations generate shear in the pycnocline that is rotating anticyclonic (clockwise Northern Hemisphere) with the inertial period. The periodic alignment of wind-induced inertial oscillation and tidal shear can yield intermittent shear spikes with enhanced turbulence production inside the pycnocline (Burchard & Rippeth, 2009). Williams et al. (2013) demonstrated for a deep shelf site in the Celtic Sea ($H > 100$ m) that these intermittent mixing events associated with inertial oscillations are a major contribution to the turbulent nitrate flux into the base of the thermocline. Significant inertial oscillations can also be seen in our simulations following the wind event on day 221 (see Figure 6h); however, during calm conditions their effect appears to be small compared to the already strong shear induced by the tides alone.

7.4. Horizontal Density Gradients

The vicinity of significant horizontal density gradients may add further complications to the turbulence generation at the base of the pycnocline. In Section 3.2, we briefly mentioned the tidal asymmetry in the BML dissipation pattern is visible in the observations. Despite comparable tidal current strengths, every other of the quarter-diurnal dissipation peaks do not reach from the bottom all the way up to the base of the pycnocline (Figure 5f). Since this behavior is not seen in the simulations (Figure 5e), it is likely due to an effect not accounted for in the model.

A likely explanation for the tidal asymmetry is the horizontal density gradients that are differentially advected by the tidal currents in a process called tidal straining (Becherer et al., 2011; Simpson et al., 1990). This process causes weak periodic stratification in the BML during a certain fraction of the tidal cycle. Stratification suppresses the vertical turbulent transport and thereby effectively insulates the base of the pycnocline from bottom-generated turbulence for half of each tidal cycle. It is not clear what overall effect this has on the average turbulence production at the base of the pycnocline. This effect may strongly vary depending on the strength and orientation of the horizontal density gradients relative to the tidal currents. We did not attempt to replicate this behavior in

the model, by imposing an arbitrary horizontal gradient, since here we are just interested in the basic mechanisms involved in generating turbulence at the base of the pycnocline. Nevertheless, investigating this particular effect on pycnocline mixing in tidally dominated shelf seas could be an interesting subject for further studies.

7.5. Boundary Layer and Polarity

In Section 5, we established that the polarity of the tidal currents is the key factor for sufficient TKE production at the base of the pycnocline. In contrast to the cyclonic component, the boundary layer from the anticyclonic (clockwise, Northern Hemisphere) component reaches all the way up to the pycnocline, where it generates substantial shear and thus TKE production. Naively, one might therefore be tempted to disregard the cyclonic tidal component when considering tidal shear at the pycnocline. However, it is important to keep in mind that it is not possible to regard the boundary layers of the two tidal components (δ_- , δ_+) as separated from each other. In reality, they nonlinearly interact with each other via the turbulent viscosity, $\delta_- \sim \sqrt{\nu_t} \sim \delta_+$. This means that even a less strong anticyclonic tidal component can result in substantial shear across the pycnocline if supported by its relatively stronger cyclonic counterpart.

Another parameter to consider is the height of the pycnocline (h_{pc}) above the bottom relative to δ_- and δ_+ . The situation described here corresponds to $\delta_- > h_{pc} > \delta_+$, which resulted in strong shear at the pycnocline from the anticyclonic ($-$) component. In a different situation, where the pycnocline is much closer to the bottom ($\delta_- > \delta_+ > h_{pc}$), both components can result in substantial shear at the pycnocline. However, it is questionable, if such a situation is sustainable for a longer time. It is more likely that the pycnocline will quickly disappear entirely when that closes the bed. Finally, we can consider a relatively deep water column compared to the tidal boundary layer ($h_{pc} > \delta_- > \delta_+$), which would yield no significant tidal shear across the pycnocline. In such a case, other processes likely dominate over tidal shear in terms of pycnocline mixing. However, on tidally dominated shelves in mid-latitude regions ($\delta_- \gg \delta_+$) with an existing seasonal pycnocline, $\delta_- > h_{pc} > \delta_+$ is the most likely scenario, which makes our findings relevant for many regions in the world.

8. Conclusions

From observations obtained during summer 2014 in the German Bight, we identify a clear SCM existing at the base of the seasonal pycnocline during calm weather conditions. Colocated is a local maximum in the dissipation of turbulent kinetic energy, which potentially provides the necessary nutrient fluxes from the BML into the lower part of the stratified pycnocline.

To study the dynamics involved in creating this peak in dissipation, we use a one-dimensional water-column model with a state-of-the-art turbulence closure. Using realistic surface and interior current forcing, the model is able to reproduce the observed density, current, and dissipation structure. Several idealized setups help to discriminate between several forcing mechanisms in terms of their contribution to mixing at the base of the pycnocline. Based on these simulations, we draw the following conclusions:

1. Bottom-generated turbulence alone cannot provide diapycnal fluxes from the bottom mixed layer into the pycnocline.
2. Local shear instabilities are the major source of diapycnal fluxes into the base of the pycnocline and hence, likely a major fuel pump for the SCM.
3. The barotropic tide alone is able to provide sufficient shear at the base of the pycnocline to generate these local shear instabilities.
4. Most of the turbulent shear production at the base of the pycnocline can be attributed to the M_2 tidal constituent.
5. Besides the amplitude of the M_2 tide, its polarity is key for generating turbulence at the pycnocline base, where the anticyclonic (clockwise, Northern Hemisphere) component of the tide dominates the shear production of turbulent kinetic energy.
6. During calm weather conditions, the wind is of minor importance for turbulence at the base of the pycnocline. However, there are indications that it still provides some extra diapycnal flux due to nonlinear interaction with the tides.

In the German Bight, a tidally dominated system, we find that the barotropic tide alone is sufficient to provide substantial diapycnal fluxes from the bottom mixed layer into the lower pycnocline, the habitat of the phytoplankton that constitutes the SCM. It is important to note that our study site is only about 40 m deep and subject to comparatively weak internal wave forcing. This is quite typical for the inner North Sea. However, at deeper shelf sites with strong internal wave forcing, the elevated role of the barotropic tide in generating shear instabilities at the pycnocline base may be challenged by other processes, for instance, internal waves and inertial oscillations.

Tidal currents can easily be predicted around the world. If the existence of the SCM is as strongly linked to the tidal currents and its polarity, as suggested by our study, it seems worth exploring this mechanism further in a broader parameter space in order to allow for extrapolation to other world regions. While this is beyond the scope of this paper, we intend to explore this further in a follow-up study.

Data Availability Statement

The glider and the ADCP data, and the respective metadata are available in the Zenodo repository at <https://doi.org/10.5281/zenodo.3525787>. The surface chlorophyll data are available from NASA at <https://oceancolor.gsfc.nasa.gov/l3/>. The climatology on nutrient data is available at <https://www.cen.uni-hamburg.de/icdc/data/ocean/nsbc.html>. Source code and model setups are available from the corresponding author on request. The model itself can be downloaded from gotm.net.

Acknowledgments

The authors gratefully acknowledge funding from the Helmholtz Association through the PoF-IV programme. The authors are grateful to Editor Arvind Singh and four anonymous reviewers for their valuable comments.

References

- Becherer, J., Burchard, H., Flöser, G., Mohrholz, V., & Umlauf, L. (2011). Evidence of tidal straining in well-mixed channel flow from micro-structure observations. *Geophysical Research Letters*, *38*(17). <https://doi.org/10.1029/2011gl049005>
- Becherer, J., Moum, J. N., Calantoni, J., Colosi, J. A., Colosi, J. A., Lerczak, J. A., et al. (2021a). Saturation of the internal tide over the inner continental shelf. Part I: Observations. *Journal of Physical Oceanography*, *51*(8), 2553–2563. <https://doi.org/10.1175/JPO-D-20-0264.1>
- Becherer, J., Moum, J. N., Calantoni, J., Colosi, J. A., Colosi, J. A., Lerczak, J. A., et al. (2021b). Saturation of the internal tide over the inner continental shelf. Part II: Parameterization. *Journal of Physical Oceanography*, *51*(8), 2565–2582. <https://doi.org/10.1175/JPO-D-21-0047.1>
- Berx, B., & Hughes, S. L. (2009). Climatology of surface and near-bed temperature and salinity on the north-west European continental shelf for 1971–2000. *Continental Shelf Research*, *29*(19), 2286–2292. <https://doi.org/10.1016/j.csr.2009.09.006>
- Bianchi, A. A., Bianucci, L., Piola, A. R., Pino, D. R., Schloss, I., Poisson, A., & Balestrini, C. F. (2005). Vertical stratification and air-sea CO₂ fluxes in the Patagonian shelf. *Journal of Geophysical Research*, *110*(C7), C07003. <https://doi.org/10.1029/2004jc002488>
- Borges, A., Delille, B., & Frankignoulle, M. (2005). Budgeting sinks and sources of CO₂ in the coastal ocean: Diversity of ecosystems counts. *Geophysical Research Letters*, *32*(14). <https://doi.org/10.1029/2005gl023053>
- Burchard, H. (1999). Recalculation of surface slopes as forcing for numerical water column models of tidal flow. *Applied Mathematical Modelling*, *23*(10), 737–755. [https://doi.org/10.1016/s0307-904x\(99\)00008-6](https://doi.org/10.1016/s0307-904x(99)00008-6)
- Burchard, H., & Baumert, H. (1995). On the performance of a mixed-layer model based on the κ - ϵ turbulence closure. *Journal of Geophysical Research*, *100*(C5), 8523–8540. <https://doi.org/10.1029/94jc03229>
- Burchard, H., & Bolding, K. (2001). Comparative analysis of four second-moment turbulence closure models for the oceanic mixed layer. *Journal of Physical Oceanography*, *31*(8), 1943–1968. [https://doi.org/10.1175/1520-0485\(2001\)031<1943:caofsm>2.0.co;2](https://doi.org/10.1175/1520-0485(2001)031<1943:caofsm>2.0.co;2)
- Burchard, H., Bolding, K., Rippeth, T. P., Stips, A., Simpson, J. H., & Sündermann, J. (2002). Microstructure of turbulence in the northern North Sea: A comparative study of observations and model simulations. *Journal of Sea Research*, *47*(3–4), 223–238. [https://doi.org/10.1016/s1385-1101\(02\)00126-0](https://doi.org/10.1016/s1385-1101(02)00126-0)
- Burchard, H., & Hetland, R. D. (2010). Quantifying the contributions of tidal straining and gravitational circulation to residual circulation in periodically stratified tidal estuaries. *Journal of Physical Oceanography*, *40*(6), 1243–1262. <https://doi.org/10.1175/2010jpo4270.1>
- Burchard, H., & Rippeth, T. P. (2009). Generation of bulk shear spikes in shallow stratified tidal seas. *Journal of Physical Oceanography*, *39*(4), 969–985. <https://doi.org/10.1175/2008jpo4074.1>
- Cullen, J. J. (2015). Subsurface chlorophyll maximum layers: Enduring enigma or mystery solved? *Annual Review of Marine Science*, *7*(1), 207–239. <https://doi.org/10.1146/annurev-marine-010213-135111>
- Egbert, G., & Ray, R. (2000). Significant dissipation of tidal energy in the deep ocean inferred from satellite altimeter data. *Nature*, *405*(6788), 775–778. <https://doi.org/10.1038/35015531>
- Fairall, C., Bradley, E., Hare, J., Grachev, A., & Edson, J. (2003). Bulk parameterization of air–sea fluxes: Updates and verification for the COARE algorithm. *Journal of Climate*, *16*(4), 571–591. [https://doi.org/10.1175/1520-0442\(2003\)016<0571:bpoasf>2.0.co;2](https://doi.org/10.1175/1520-0442(2003)016<0571:bpoasf>2.0.co;2)
- Fer, I., Peterson, A. K., & Ullgren, J. E. (2014). Microstructure measurements from an underwater glider in the turbulent faroe bank channel overflow. *Journal of Atmospheric and Oceanic Technology*, *31*(5), 1128–1150. <https://doi.org/10.1175/JTECH-D-13-00221.1>
- Ferrari, R., & Wunsch, C. (2009). Ocean circulation kinetic energy: Reservoirs, sources, and sinks. *Annual Review of Fluid Mechanics*, *41*(1), 253–282. <https://doi.org/10.1146/annurev.fluid.40.111406.102139>
- Green, J., Simpson, J., Thorpe, S., & Rippeth, T. (2010). Observations of internal tidal waves in the isolated seasonally stratified region of the Western Irish Sea. *Continental Shelf Research*, *30*(2), 214–225. <https://doi.org/10.1016/j.csr.2009.11.004>
- Hinrichs, I., Gouretski, V., Pätsch, J., Emeis, K.-C., & Stammer, D. (2017). North Sea biogeochemical climatology (version 1.1). https://doi.org/10.1594/WDCC/NSBclim_v1.1
- Hopkins, J. E., Palmer, M. R., Poulton, A. J., Hickman, A. E., & Sharples, J. (2021). Control of a phytoplankton bloom by wind-driven vertical mixing and light availability. *Limnology & Oceanography*, *66*(5), 1926–1949. <https://doi.org/10.1002/lno.11734>
- Inall, M. E., Rippeth, T. P., & Sherwin, T. J. (2000). Impact of nonlinear waves on the dissipation of internal tidal energy at a shelf break. *Journal of Geophysical Research*, *105*(C4), 8687–8705. <https://doi.org/10.1029/1999jc900299>

- Kaspar, F., Niermann, D., Borsche, M., Fiedler, S., Keller, J., Potthast, R., et al. (2020). Regional atmospheric reanalysis activities at deutscher wetterdienst: Review of evaluation results and application examples with a focus on renewable energy. *Advances in Science and Research*, 17, 115–128. <https://doi.org/10.5194/asr-17-115-2020>
- Li, Q., Bruggeman, J., Burchard, H., Klingbeil, K., Umlauf, L., & Bolding, K. (2021). Integrating CVMix into GOTM (v6. 0): A consistent framework for testing, comparing, and applying ocean mixing schemes. *Geoscientific Model Development*, 14(7), 4261–4282. <https://doi.org/10.5194/gmd-14-4261-2021>
- Lincoln, B., Rippeth, T., & Simpson, J. (2016). Surface mixed layer deepening through wind shear alignment in a seasonally stratified shallow sea. *Journal of Geophysical Research*, 121(8), 6021–6034. <https://doi.org/10.1002/2015jc011382>
- Lueck, R. G., Wolk, F., & Yamazaki, H. (2002). Oceanic velocity microstructure measurements in the 20th century. *Journal of Oceanography*, 58(1), 153–174. <https://doi.org/10.1023/a:1015837020019>
- Maas, L. R. M., & van Haren, J. J. M. (1987). Observations on the vertical structure of tidal and inertial currents in the central North Sea. *Journal of Marine Research*, 45(2), 293–318. <https://doi.org/10.1357/002224087788401106>
- MacKinnon, J., & Gregg, M. (2003). Mixing on the late-summer New England shelf – Solibores, shear, and stratification. *Journal of Physical Oceanography*, 33(7), 1476–1492. [https://doi.org/10.1175/1520-0485\(2003\)033<1476:modne>2.0.co;2](https://doi.org/10.1175/1520-0485(2003)033<1476:modne>2.0.co;2)
- Moore, C. M., Suggett, D. J., Hickman, A. E., Kim, Y.-N., Tweddle, J. F., Sharples, J., et al. (2006). Phytoplankton photoacclimation and photoadaptation in response to environmental gradients in a shelf sea. *Limnology & Oceanography*, 51(2), 936–949. <https://doi.org/10.4319/lo.2006.51.2.0936>
- Moum, J., Farmer, D., Smyth, W., Armi, L., & Vagle, S. (2003). Structure and generation of turbulence at interfaces strained by internal solitary waves propagating shoreward over the continental shelf. *Journal of Physical Oceanography*, 33(10), 2093–2112. [https://doi.org/10.1175/1520-0485\(2003\)033<2093:sagota>2.0.co;2](https://doi.org/10.1175/1520-0485(2003)033<2093:sagota>2.0.co;2)
- Muller-Karger, F. E., Varela, R., Thunell, R., Luerssen, R., Hu, C., & Walsh, J. J. (2005). The importance of continental margins in the global carbon cycle. *Geophysical Research Letters*, 32(1), L01602. <https://doi.org/10.1029/2004gl021346>
- NASA Ocean Biology Processing Group. (2017). Modis-aqua level 3 mapped chlorophyll data version 2018.0. NASA Ocean Biology DAAC. Retrieved from <https://doi.org/10.5067/AQUA/MODIS/L3M/CHL/2018> <https://oceancolor.gsfc.nasa.gov/data/10.5067/AQUA/MODIS/L3M/CHL/2018>
- Osborn, T. (1980). Estimates of the local rate of vertical diffusion from dissipation measurements. *Journal of Physical Oceanography*, 10(1), 83–89. [https://doi.org/10.1175/1520-0485\(1980\)010<0083:eotlro>2.0.co;2](https://doi.org/10.1175/1520-0485(1980)010<0083:eotlro>2.0.co;2)
- Palmer, M. R., Rippeth, T. P., & Simpson, J. H. (2008). An investigation of internal mixing in a seasonally stratified shelf sea. *Journal of Geophysical Research*, 113(C12). <https://doi.org/10.1029/2007jc004531>
- Prandle, D. (1982). The vertical structure of tidal currents and other oscillatory flows. *Continental Shelf Research*, 1(2), 191–207. [https://doi.org/10.1016/0278-4343\(82\)90004-8](https://doi.org/10.1016/0278-4343(82)90004-8)
- Richardson, K., Visser, A., & Pedersen, F. B. (2000). Subsurface phytoplankton blooms fuel pelagic production in the North Sea. *Journal of Plankton Research*, 22(9), 1663–1671. <https://doi.org/10.1093/plankt/22.9.1663>
- Rippeth, T., Lincoln, B., Kennedy, H., Palmer, M., Sharples, J., & Williams, C. (2014). Impact of vertical mixing on sea surface pCO₂ in temperate seasonally stratified shelf seas. *Journal of Geophysical Research*, 119(6), 3868–3882. <https://doi.org/10.1002/2014jc010089>
- Rippeth, T. P. (2005). Mixing in seasonally stratified shelf seas: A shifting paradigm. *Philosophical Transactions of the Royal Society A: Mathematical, Physical & Engineering Sciences*, 363(1837), 2837–2854. <https://doi.org/10.1098/rsta.2005.1662>
- Rippeth, T. P., Palmer, M. R., Simpson, J. H., Fisher, N. R., & Sharples, J. (2005). Thermocline mixing in summer stratified continental shelf seas. *Geophysical Research Letters*, 32(5), L05602. <https://doi.org/10.1029/2004gl022104>
- Rippeth, T. P., Wiles, P., Palmer, M. R., Sharples, J., & Tweddle, J. (2009). The diapycnal nutrient flux and shear-induced diapycnal mixing in the seasonally stratified Western Irish Sea. *Continental Shelf Research*, 29(13), 1580–1587. <https://doi.org/10.1016/j.csr.2009.04.009>
- Schultze, L. K., Merckelbach, L. M., & Carpenter, J. R. (2017). Turbulence and mixing in a shallow shelf sea from underwater gliders. *Journal of Geophysical Research*, 122(11), 9092–9109. <https://doi.org/10.1002/2017jc012872>
- Schultze, L. K., Merckelbach, L. M., & Carpenter, J. R. (2020). Storm-induced turbulence alters shelf sea vertical fluxes. *Limnology and Oceanography Letters*, 5(3), 264–270. <https://doi.org/10.1002/lo12.10139>
- Sharples, J. (2007). Potential impacts of the spring-neap tidal cycle on shelf sea primary production. *Journal of Plankton Research*, 30(2), 183–197. <https://doi.org/10.1093/plankt/fbm088>
- Sharples, J., Moore, C. M., & Abraham, E. R. (2001). Internal tide dissipation, mixing, and vertical nitrate flux at the shelf edge of NE New Zealand. *Journal of Geophysical Research*, 106(C7), 14069–14081. <https://doi.org/10.1029/2000jc000604>
- Sharples, J., Moore, C. M., Rippeth, T. P., Holligan, P. M., Hydes, D. J., Fisher, N. R., & Simpson, J. H. (2001). Phytoplankton distribution and survival in the thermocline. *Limnology & Oceanography*, 46(3), 486–496. <https://doi.org/10.4319/lo.2001.46.3.0486>
- Sharples, J., & Zeldis, J. R. (2019). Variability of internal tide energy, mixing and nitrate fluxes in response to changes in stratification on the northeast New Zealand continental shelf. *New Zealand Journal of Marine & Freshwater Research*, 55, 1–18. <https://doi.org/10.1080/00288330.2019.1705357>
- Simpson, J. H., Brown, J., Matthews, J., & Allen, G. (1990). Tidal straining, density currents, and stirring in the control of estuarine stratification. *Estuaries*, 13(2), 125–132. <https://doi.org/10.2307/1351581>
- Simpson, J. H., Burchard, H., Fisher, N. R., & Rippeth, T. P. (2002). The semi-diurnal cycle of dissipation in a rofi: Model-measurement comparisons. *Continental Shelf Research*, 22(11–13), 1615–1628. [https://doi.org/10.1016/s0278-4343\(02\)00025-0](https://doi.org/10.1016/s0278-4343(02)00025-0)
- Simpson, J. H., Crawford, W. R., Rippeth, T. P., Campbell, A. R., & Cheok, J. V. S. (1996). The vertical structure of turbulent dissipation in shelf seas. *Journal of Physical Oceanography*, 26(8), 1579–1590. [https://doi.org/10.1175/1520-0485\(1996\)026<1579:tvstod>2.0.co;2](https://doi.org/10.1175/1520-0485(1996)026<1579:tvstod>2.0.co;2)
- Simpson, J. H., & Tinker, J. P. (2009). A test of the influence of tidal stream polarity on the structure of turbulent dissipation. *Continental Shelf Research*, 29(1), 320–332. <https://doi.org/10.1016/j.csr.2007.05.013>
- Souza, A., & Simpson, J. (1996). The modification of tidal ellipses by stratification in the Rhine ROFI. *Continental Shelf Research*, 16(8), 997–1007. [https://doi.org/10.1016/0278-4343\(95\)00042-9](https://doi.org/10.1016/0278-4343(95)00042-9)
- Thomas, H., Bozec, Y., Elkalay, K., & De Baar, H. J. (2004). Enhanced open ocean storage of CO₂ from Shelf Sea pumping. *Science*, 304(5673), 1005–1008. <https://doi.org/10.1126/science.1095491>
- Tsunogai, S., Watanabe, S., & Sato, T. (1999). Is there a “continental shelf pump” for the absorption of atmospheric CO₂? *Tellus B: Chemical and Physical Meteorology*, 51(3), 701–712. <https://doi.org/10.1034/j.1600-0889.1999.t01-2-00010.x>
- Umlauf, L. (2009). The description of mixing in stratified layers without shear in large-scale ocean models. *Journal of Physical Oceanography*, 39(11), 3032–3039. <https://doi.org/10.1175/2009jpo4006.1>
- Umlauf, L., & Burchard, H. (2005). Second-order turbulence closure models for geophysical boundary layers. A review of recent work. *Continental Shelf Research*, 25(7–8), 795–827. <https://doi.org/10.1016/j.csr.2004.08.004>

- van Haren, H. (2000). Properties of vertical current shear across stratification in the North Sea. *Journal of Marine Research*, 58(3), 465–491. <https://doi.org/10.1357/002224000321511115>
- van Haren, H., Maas, L., Zimmerman, J., Ridderinkhof, H., & Malschaert, H. (1999). Strong inertial currents and marginal internal wave stability in the central North Sea. *Geophysical Research Letters*, 26(19), 2993–2996. <https://doi.org/10.1029/1999gl002352>
- van Leeuwen, S., Tett, P., Mills, D., & van der Molen, J. (2015). Stratified and nonstratified areas in the north sea: Long-term variability and biological and policy implications. *Journal of Geophysical Research*, 120(7), 4670–4686. <https://doi.org/10.1002/2014jc010485>
- Williams, C., Sharples, J., Mahaffey, C., & Rippeth, T. (2013). Wind-driven nutrient pulses to the subsurface chlorophyll maximum in seasonally stratified shelf seas. *Geophysical Research Letters*, 40(20), 5467–5472. <https://doi.org/10.1002/2013gl058171>
- Wolk, F., Yamazaki, H., Seuront, L., & Lueck, R. G. (2002). A new free-fall profiler for measuring biophysical microstructure. *Journal of Atmospheric and Oceanic Technology*, 19(5), 780–793. [https://doi.org/10.1175/1520-0426\(2002\)019<0780:anffpf>2.0.co;2](https://doi.org/10.1175/1520-0426(2002)019<0780:anffpf>2.0.co;2)